Biomaterials Science

Accepted Manuscript

This article can be cited before page numbers have been issued, to do this please use: L. Sun, Q. Li, L. Zhang, H. Chai, L. Yu, Z. Xu, Y. Kang and P. Xue, *Biomater. Sci.*, 2019, DOI: 10.1039/C9BM00351G.

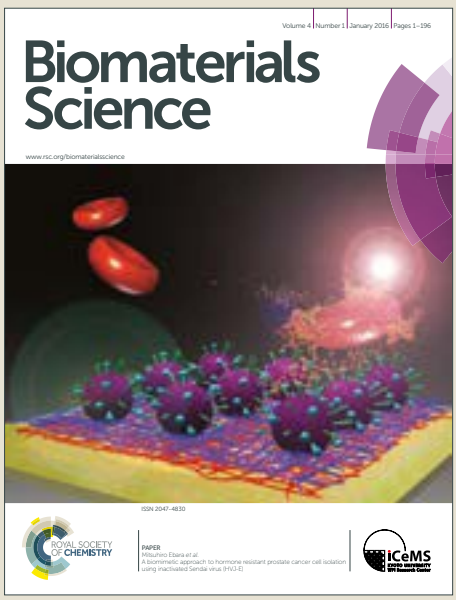

ROYAL SOCIETY OF CHEMISTRY

rsc.li/biomaterials-science

View Article Online
DOI: 10.1039/C9BM00351G

Stimuli Responsive PEGylated Bismuth Selenide Hollow Nanocapsules for Fluorescence/CT imaging and Light-Driven Multimodal Tumor Therapy

Lihong Sun [a, b], Qian Li [a, b], Lei Zhang [c], Huihui Chai [a, b], Ling Yu [a, b], Zhigang Xu [a, b], Yuejun Kang [a, b], Peng Xue [a, b*]

[a] Key Laboratory of Luminescent and Real-Time Analytical Chemistry (Southwest University), Ministry of Education, School of Materials and Energy, Southwest University, Chongqing 400715, China. E-mails: xuepeng@swu.edu.cn (P. Xue)

[b] Chongqing Engineering Research Center for Micro-Nano Biomedical Materials and Devices, Southwest University, Chongqing 400715, China.

[c] Institute of Sericulture and System Biology, Southwest University, Chongqing 400716, China.

†Electronic supplementary information (ESI) available.

View Article Online
DOI: 10.1039/C9BM00351G

Abstract

Stimuli-responsive therapeutic nanosystems exhibit enhanced selectivity and higher biosafety for cancer theranostics via recognizing exogenous or endogenous tumor-associated factors. Herein, we developed a multifunctional nanocomplex (Bi_2Se_3@PEG/DOX/Ce6 nanocapsules, or BPDC NCs in brief) that was constructed by loading chlorin e6 (Ce6) and doxorubicin (DOX) into PEGylated hollow bismuth sulfide nanocapsules. Upon the administration of BPDC NCs, composite laser irradiation can effectively activate the local hyperthermia generation and the yield of cytotoxic reactive oxygen species (ROS). In another aspect, on-demand drug release can be triggered in mild acidic tumor microenvironment or by thermal shock. Moreover, imaging navigation with respect to infrared thermography, computed tomography (CT) and fluorescence imaging and may potentially monitor the biodistribution of BPDC NCs, thanks to the local hyperthermia generation, fluorescence emission of Ce6 and high Z-element of bismuth. Finally, we demonstrated the tumor site-specific photothermal therapy (PTT), photodynamic therapy (PDT) and chemotherapeutic effects for high efficacious tumor suppression with minimized systemic toxicity. Taken together, these findings indeed provide insights of broadening the application of Bi_2Se_3 nanocapsules for cancer management and precision medicine.

Keywords

Bismuth selenide hollow nanocapsules; multimodal therapy; controlled drug release; light-driven therapy.

View Article Online
DOI: 10.1039/C9BM00351G

Introduction

Nanoparticles (NPs) have emerged as attractive drug carriers for intracellular delivery in the field of nanomedicine.[1, 2] To achieve an optimum antitumor efficacy, vast types of NPs have been developed to enhance the intracellular delivery of antineoplastic agents, including chemotherapeutic drugs, photosensitizers, siRNA and antibodies through targeted tumor accumulation, specific endocytosis, as well as drug translocation pathway, et al.[3-6] In particular, stimuli-responsive NPs, which can be smartly switched from "a resting state" to "an activated state" upon reaching tumor site and release their payload within the tumor, responding to either exogenous stimulus (e.g., light, temperature or acoustic wave) or endogenous stimulus (e.g., variations in pH, enzyme or redox), have been extensively exploited in recent years.[7-10] Moreover, multiple stimuli are capable of synergistically activating drug-laden NPs, thereby facilitating precise spatiotemporal implementation of cancer treatment to minimize the adverse side effects toward normal tissues.[11-13] Thereby, the development of stimuli-responsive NPs with excellent biocompatibility holds a great promise for new generations of combinatorial tumor therapies based on high efficient and targeted intracellular delivery of therapeutic molecules. In another aspect, the integration of imaging, targeting and treatment modalities into a single NP formulation has been widely exploited for customized cancer diagnosis and therapy in terms of the following areas: targeted delivery of therapeutic agents, monitoring the biodistribution and target site accumulation, detection of tumor-specific biomarkers, imageological diagnosis of tumor and metastases, predict a potential treatment response, and real-time tracking the treatment outcome.[14-16] In most cases, multiple components corresponding to diversified imaging and therapeutic modes are

View Article Online
DOI: 10.1039/C9BM00351G

requested to compensate the inherent restriction of each single modality.[17] In spite of many researches on the development of multifunctional NPs, a huge unmet medical demands in cancer theranosics remains substantially significant. Therefore, the development of functional NPs with long-term stability upon circulation, high efficient drug dose, on-demand drug release, decent biocompatibility together with high-contrast imaging property is incredibly crucial for realizing high performance tumor detection and avoiding the requirements for multiple doses.

In recent years, bismuth chalcogenides nanomaterials, bismuth selenide (Bi_2Se_3) NPs in particular, have attracted increasing attentions owing to their intriguing surface electronic states as a topological insulator.[18, 19] More attractively, Bi_2Se_3 NPs also possess great potential in biomedical applications, attributed to the high photoelectric absorption coefficient of Bi and the antitumor activity of Se element.[20] Meanwhile, strong hyperthermia-induced tumor ablation using Bi_2Se_3 NPs have been demonstrated, attributed to their high photothermal conversion efficiency, implying their good potency for photothermal therapy (PTT).[21-23] As the most prevalently used diagnostic method in clinics, computed tomography (CT) is evolved as an imaging modality with ultra-high spatiotemporal resolution and non-invasiveness.[24, 25] Contrast agents containing heavier elements (higher atomic number [Z]) usually offer higher image contrast at equal mass concentration. Bi can be regarded as a typical high-Z element (I, 53; Gd, 64; Ta, 73; Bi, 83) with a corresponding X-ray attenuation coefficient (I, 1.94; Gd, 2.29; Ta, 4.3, Bi, 5.74 $cm^2 \cdot kg^{-1}$ at 100 KeV).[26, 27] Thus, contrast agent with bismuth content, such as bismuth-derived NPs, have been recently investigated for enhanced CT. [28-30] However, drug loading efficiency of solid Bi_2Se_3 NPs is considerably low due to their limited

View Article Online
DOI: 10.1039/C9BM00351G

surface area, which is inferior for delivering efficacious dose of drug into the tumor area. Alternatively, Li et al. reported a highly porous Bi_2Se_3 sponge with expanded surface area for encapsulating chemotherapeutic drugs to achieve synergistic thermo-chemotherapy.[31] In spite of the current superiorities, *in vivo* stability and biocompatibility of mesoporous Bi_2Se_3 NPs is in urgent need to be improved for efficiently targeting to tumor area through enhanced permeability and retention (EPR) effect. Moreover, it is still essential for Bi_2Se_3 NPs to couple with other functional modalities for cancer theranostics.

Photodynamic therapy (PDT) has emerged as a reliable and noninvasive therapeutic strategy for adjuvant treatment of cancer or other diseases.[32-34] The realization of PDT relies on three fundamental factors: photosensitizer, light with a specific optical wavelength and molecular oxygen. Photosensitizers are responsible for the absorption of light energy and transform the surrounding molecular oxygen into cytotoxic reactant oxygen species (ROS). However, traditional photosensitizers exhibit poor tumor selectivity, which might damage the normal tissues upon laser exposure.[35] Chlorin e6 (Ce6) have been attracting tremendous interests as a PDT agent with near infrared (NIR) fluorescence emission and high singlet oxygen quantum yield.[36, 37] However, free Ce6 molecules are incapable of effective tumor targeting, resulting in a rapid degradation and blood clearance during long-term circulation. Moreover, Ce6 molecules may spontaneously aggregate into larger crystals under aqueous condition, prohibiting efficient cellular uptake through endocytosis.[38] Fortunately, drug nanocarriers provide an alternative option for steadily delivering Ce6 molecules intracellularly within the tumor site after intravenous (i.v.) injection.[39-41] To retain therapeutic potency and reduce

View Article Online
DOI: 10.1039/C9BM00351G

potential adverse effects, PDT agents take effects specifically within the tumor area when being activated by manually exogenous stimuli or tumor-associated endogenous stimuli.[42]

In this study, we developed a multifunctional nanoagent platform on the basis of hollow mesoporous Bi_2Se_3 nanocapsules (NCs) for fluorescence/CT bimodal imaging and chem/photothermal/photodynamic combination therapy of cancer. Bi_2Se_3 NCs were synthesized through a controlled self-etching reaction in the presence of PVP.[21] Therapeutic molecules, including Ce6 as the PDT agent and doxorubicin (DOX) as a typical chemotherapeutic drug, were encapsulated into the tiny pores and hollow cavity of Bi_2Se_3 NCs to form Bi_2Se_3@PEG/DOX/Ce6 (BPDC NCs). Taking advantage of the unique properties of Ce6 component, BPDC NCs can be used not only for fluorescence imaging via external excitation to reveal *in vivo* biodistribution but also for targeted PDT with high efficiency. Moreover, Polyethylene glycol (PEG) as the capping agent was conjugated onto the surface of Bi_2Se_3 NPs to enhance the biocompatibility and physiological stability as well as stabilizing the encapsulated functional molecules. Thus, the integration of Ce6 and PEG endows Bi_2Se_3 NCs with unique advantages for achieving an improved performance both in tumor diagnosis and therapy, as well as long-term stability in blood circulation, which are regarded as substantial progress on the basis of primary studies.[21, 31] Importantly, Bi_2Se_3 NCs, as the framework, serves as the photothermal agent as well as CT imaging contrast agent. The release of loading content from nanocarriers can be effectively triggered by the local hyperthermia and mild acidic tumor microenvironment when the nanodrug being concentrated within the tumor region via EPR effect. Upon NIR laser irradiation, photothermal tumor ablation and drug release were implemented intracellularly, followed by the subsequent PDT/chemotherapy subject

View Article Online
DOI: 10.1039/C9BM00351G

to a secondary laser irradiation. In another aspect, high-resolution fluorescence/CT dual-modal imaging were accomplished to supply the accurate diagnostic information for tumor therapy (Fig. 1). Such safe and reliable nanoagents, serving as a "one-for-all" theranostic platform, could provide multiple modalities for stimuli-responsive tumor therapeutics and bimodal imaging diagnostics.

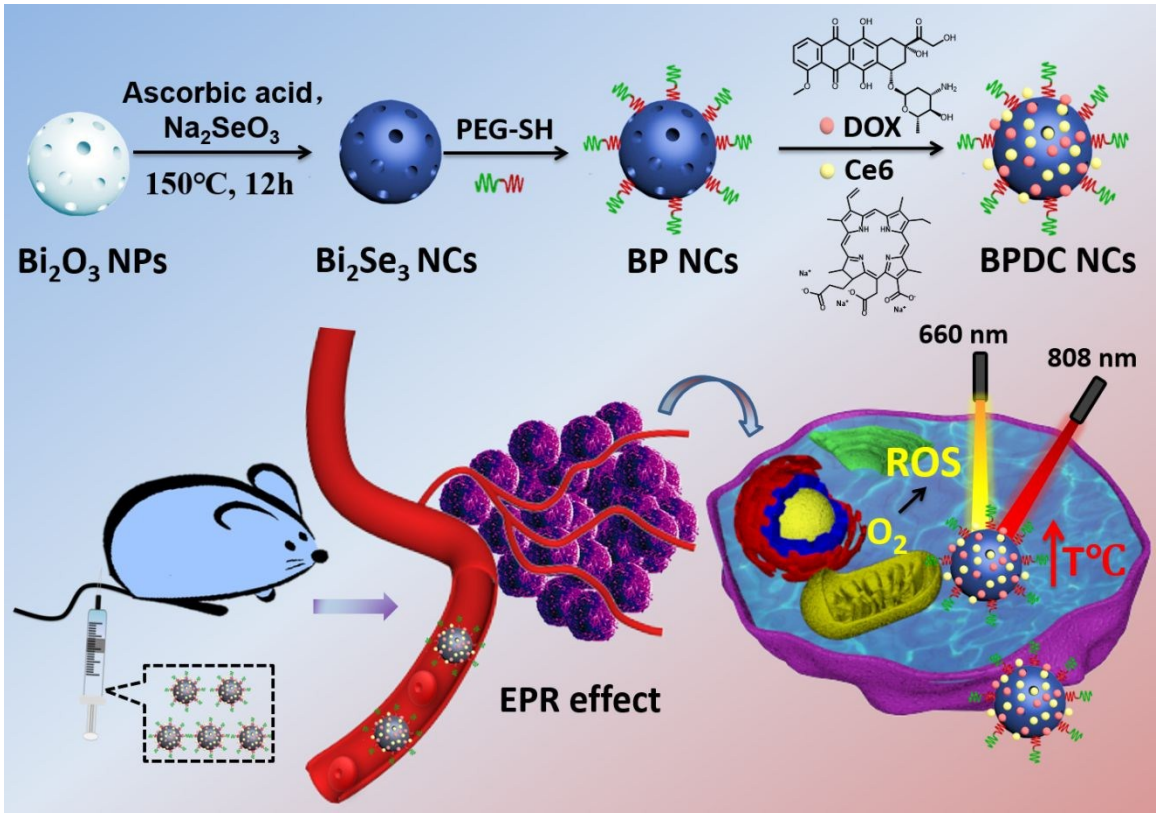

Fig. 1. Scheme of the synthetic route of mesoporous hollow BPDC NCs as a multifunctional and versatile biomedical platform for tumor theranostics.

Experimental

Materials

View Article Online
DOI: 10.1039/C9BM00351G

Sodium hydroxide (NaOH, ⩾97.0%), Bismuth nitrate pentahydrate ($Bi(NO_3)_3 \cdot 5H_2O$, ⩾ 99.99%), poly-vinylpyrrolidone (PVP, Mw ≈ 10000 Da), ethylene glycol (EG, >99%), ascorbic acid (AA, ⩾99%), dimethyl sulfoxide (DMSO) and MTT cell viability assay kit were purchased from Shanghai Aladdin Bio-Chem Technology Co., LTD (China). Sodium selenite (Na_2SeO_4, ⩾95%) was supplied by Sigma-Aldrich (USA). Nitric acid (HNO_3, 70%) was obtained from Tianjin Fengchuan Chemical Reagent Technologies Co. Ltd (China). Chlorin e6 (Ce6, 93~98%) was provided by Frontier Scientific, InC (USA). Thiol−polyethylene glycol (SH-PEG, Mw=2000Da) was purchased from Xi'an Ruixi Biological Technology Co. Ltd (China). Dulbecco's modified eagle's medium (DMEM), penicillin (10,000 $U \cdot mL^{-1}$)/streptomycin (10,000 $\mu g \cdot mL^{-1}$) mixture, fetal bovine serum (FBS), TrypLE™ Express Enzyme, phosphate buffered saline (1×PBS), LIVE/DEAD® viability/cytotoxicity kit, Calcein AM and ethidium Homodimer-1 (EthD-1) were acquired from Thermo Fisher Scientific (USA). JC-1 staining kit and One Step TUNEL Apoptosis Assay Kit were provided by Beyotime Biotechnology (China). KM mice and BALB/c mice models were purchased from Chongqing Teng Xin Bill Experimental Animal Sales Co. Ltd (China). Deionized (DI) water (18.2 MΩ·cm) was collected from a Milli-Q Synthesis A10 purification system (Molsheim, France).

Preparation of hollow mesoporous Bi_2Se_3@PEG NCs

Bi_2O_3 NPs were firstly synthesized as the templates based on a previously reported method.[21] Specifically, $Bi(NO_3)_3 \cdot 5H_2O$ (0.186 g) was dispersed in 5 mL HNO_3 solution (1 M). Then, NaOH (0.054 g) and EG (25 mL) were introduced into the above solution in

View Article Online
DOI: 10.1039/C9BM00351G

sequence under magnetic stirring. Afterwards, the mixture was transferred into a stainless steel autoclave with Teflon liner and maintained at 150 ℃ for 3 h. Bi_2O_3 NPs were finally obtained after purification with DI water for five times.

Bi_2Se_3 NCs were subsequently prepared based on a hydrothermal process by exploiting the previously obtained Bi_2O_3 NPs and bismuth precursor. Briefly, ascorbic acid (0.3 g) and Na_2SeO_4 powder (0.038 g) were dissolved in 5mL DI water and then mixed with Bi_2O_3 NP dispersion (5 mL) at 25°C. The mixture was then transferred into a stainless steel autoclave and maintained at 150 °C for 12 h. The obtained products were purified with DI water for five times, and dehydrated in a heating oven under vacuum at 50°C for 12 h. To conjugate PEG, 20 mg Bi_2Se_3 NCs was dispersed in 100 mL DI water, followed by adding 40 mg SH-PEG under ultrasonication. The mixture was under stirring for 12 h, followed by the removal of unconjugated SH-PEG through centrifugation and washing in DI water. The obtained hollow mesoporous Bi_2Se_3@PEG NCs were re-dispersed in DI water and stored at 4 °C for further use.

Drug loading and release

DOX and Ce6 loading into Bi_2Se_3@PEG NCs were performed by mixing Bi_2Se_3@PEG NC dispersion (5 mL, 1 $mg \cdot mL^{-1}$) with DOX (2.5 mg) and Ce6 (2.5 mg) in phosphate buffer (20×10^{-3} M) at pH = 8. After stirring for 24 h in a dark place, BPDC NCs were obtained through high-speed centrifugation at 10, 000 rpm for 10 min and washing in DI water for three time. Drug loading capacity of BPDC NCs was determined by the corresponding standard calibration curve derived from a fluorescence spectrum of DOX

View Article Online
DOI: 10.1039/C9BM00351G

or Ce6 (Ex: 405nm, Em: 660nm for Ce6; Ex: 488nm, Em: 535nm for DOX). Drug loading capacity (DLC) and encapsulation efficiency (EE) was calculated by the following equations (1) and (2):

$$\text{DLC}\ (\%) = \frac{weight\ of\ devoted\ drug - weight\ of\ drug\ in\ supernantant}{weight\ of\ BPDC\ NCs} \times 100\% \quad (1)$$

$$\text{EE}\ (\%) = \frac{weight\ of\ devoted\ drug - weight\ of\ drug\ in\ supernantant}{weight\ of\ devoted\ drug} \times 100\% \quad (2)$$

Drug release behaviors of BPDC NCs were evaluated at different pH values based on a traditional dialysis method *in vitro*. BPDC NCs (1 mL, 2 mg·mL^{-1}) was loaded into a dialysis bag (M_w=3500) and then submerged into 80mL of 1×PBS (pH = 5.0, 6.5 and 7.4) as the release system, which was under shaking at a constant speed at 37^{o}C. To monitor the releasing process, 1mL aliquot of release medium was withdrawn at predesigned time points, followed by replenishing the releasing system by fresh medium with identical volume. The amount of released DOX and Ce6 was dynamically monitored based on above-mentioned fluorescence spectrophotometry.

Characterization

The morphology of Bi_2O_3 NPs, Bi_2Se_3@PEG NCs and BPDC NCs were characterized using field emission scanning electron microscopy (FESEM, JSM-7800F, JEOL, Japan) and transmission electron microscopy (TEM, Libra 120 plus, Carl Zeiss, USA). The hydrodynamic diameter and surface potential of various agents were measured using a dynamic light scattering (DLS) analyzer (Zeta Sizer/NanoZS90). The optical absorbance was obtained from a UV-vis-NIR spectrometer (UV-1800, Shimadzu Scientific

View Article Online
DOI: 10.1039/C9BM00351G

Instruments, Japan). Fourier transform infrared (FT-IR) spectrum of NPs was measured through a FT-IR spectrophotometer (Perkin Elmer, USA). Nitrogen adsorption–desorption isotherms were measured to determine the Brunauer–Emmett–Teller (BET) surface areas and pore volumes using a Quantachrome Nova 1200e analyzer. The crystalline structure and purity of the products were analyzed by using an X-ray diffractometer (XRD-7000, Shimadzu, Japan) with CuK_{α} radiation (λ=1.5406 Å). X-ray photoelectron spectroscopy (XPS) was performed to determine the elemental composition of intermediate and final products through an X-ray photoelectron spectrometer (ESCALAB 250Xi, Thermo Fisher Scientific, USA).

NIR light-induced temperature elevation

1 mL aqueous dispersion of BPDC NCs was loaded in a 1 cm × 1 cm × 4 cm quartz cuvette cell. Then, the cuvette was irradiated by an NIR laser (wavelength: 808nm) with specific output power density and duration time. The temperature increase was recorded by using a thermal imaging camera (Fluke, TiS55) at an interval of 30 sec. The photothermal stability of BPDC NCs was assessed through four cycles of on/off NIR laser irradiation. Briefly, the sample-laden cuvette was exposed to an NIR laser for 10 min, followed by spontaneously being brought to room temperature prior to the next round irradiation.

Biocompatibility

View Article Online
DOI: 10.1039/C9BM00351G

Human umbilical vein endothelial cells (HUVECs), L929 mouse fibroblasts, HeLa cells (a human cervical cancer cell line) and 4T1 cells (a murine mammary carcinoma cell line) in this study were obtained from Cell Bank of Type Culture Collection of the Chinese Academy of Sciences (Shanghai, China). To assess the biocompatibility of Bi_2Se_3@PEG NCs, standard MTT cell viability assay were conducted using both of the L929 and HUVEC cells. Briefly, L929 and HUVEC cells were seeded in 96-well plates (5,000 cells per well), and cultured in the atmosphere of 5% CO_2 at 37 °C overnight. Afterwards, the medium was replaced by the fresh medium containing various concentrations of Bi_2Se_3@PEG NCs (0, 10, 25, 50, 100 and 200 $\mu g \cdot mL^{-1}$), and another incubation was allowed to proceed for 24 h. Thereafter, the supernatant in each well was aspirated and 200 μL of MTT solution (0.5 $mg \cdot mL^{-1}$) was subsequently added into each well. After 4 h incubation, 200 μL of DMSO was introduced to each well to replace the supernatant. Finally, the optical absorbance of each well was measured using a microplate reader (SPARK 10M) at the wavelength of 490 nm and 630nm. Cell viability was calculated based on the equation (3):

$$\text{Cell viability (\%)} = \frac{\text{OD}_{490nm}\ sample - \text{OD}_{630nm}\ sample}{\text{OD}_{490nm}\ control - \text{OD}_{630nm}\ control} \times 100\% \qquad (3)$$

Reactive oxygen species (ROS) detection

Intracellular ROS generation was detected using the DCFH-DA probe following the recommended protocol. Briefly, 4T1 or HeLa cells were seeded in 12-well culture plates (4×10^4 per well) and incubated overnight. Afterwards, the medium was replaced by free Ce6 (10 $\mu g \cdot mL^{-1}$) or Bi_2Se_3@PEG/Ce6 (BPC) NCs (the equivalent Ce6 concentration: 10

View Article Online
DOI: 10.1039/C9BM00351G

μg·mL^{-1}) dispersed in DMEM. After 4h incubation, the cells were treated by DCFH-DA (10 μM, 600 μL) for 30 min. Then, the cells were washed with 1×PBS thrice, followed by being exposed to a 660nm laser (output power = 0.76 W·cm^{-2}) for 5 min. Afterwards, the cells were stained with DAPI (1 μg·mL^{-1}, 600 μL) for 3 min, and rinsed with 1×PBS thrice. Lastly, fluorescence images of the cells after staining were acquired through laser scanning confocal microscopy (LSCM, LSM800, Zeiss, Germany).

Combined PTT/PDT effect on tumor cell destruction *in vitro*

To investigate the cell ablation performance *in vitro*, 4T1 cells and HeLa cells were initially seeded in a 24-well plate (5 × 10^4 cells per well). After incubation at 37^{o}C for 12h, the previous culture medium was replaced with fresh medium containing Bi_2Se_3@PEG NCs, free Ce6 or Bi_2Se_3@PEG/Ce6 NCs. After another 4h incubation, the cells were washed with 1×PBS thrice and then subject to 660nm laser irradiation (0.76 W·cm^{-2}) for 5 min and 808nm laser irradiation (2 W·cm^{-2}) for 5 min in sequence. Then, the cells were stained by calcein AM/EthD-1 for fluorescence imaging. To measure the mitochondrial membrane potential change induced by the photothermal/photodynamic effect, JC-1 staining was carried out according to a standard protocol from the manufacturer. After staining for 30 min, cells were thoroughly washed with 1×PBS and examined through LSCM.

Cellular uptake and internalization

View Article Online
DOI: 10.1039/C9BM00351G

Cellular uptake of Ce6 and DOX mediated by BPDC NCs was evaluated qualitatively through LSCM and quantitatively through flow cytometry. For LSCM, HeLa cells or 4T1 cells were initially seeded in a culture dish at the number of 4×10^4. After being cultured at 37°C for 12h, fresh medium containing BPDC NCs (equivalent DOX concentration: 5 $\mu g\cdot mL^{-1}$) was introduced to replace the previous medium, followed by another incubation for 1 h or 4 h. Afterwards, cells were washed with 1×PBS for three times, and fixed with 4% paraformaldehyde for 30 min. After being stained with DAPI ($1\mu g\cdot mL^{-1}$) for 3 min, the fluorescence emission from the cells was recorded through three individual band pass filters (410–481 nm, 500-590nm and 638–747 nm) and objective of LD Plan-Neofluar (20×/0.4 Korr M27) using LSCM.

For flow cytometry analysis, HeLa or 4T1 cells were firstly seeded in a 12-well cell culture plate (1×10^5 cells per well) and cultured at 37°C overnight. Then, fresh medium containing BPDC NCs (equivalent DOX concentration: 5 $\mu g\cdot mL^{-1}$) was introduced to replace the previous medium. Cell culture was allowed to proceed for 0.5 h, 1 h, 2 h, 4 h or 6 h at 37°C. Thereafter, cells were washed thrice with 1×PBS, trypsinized, centrifuged and resuspended in 400 μL of 1×PBS for analysis using a flow cytometer (Novocyte, ACEA Biosciences, US). The collected data were analytically processed using FlowJo (ver. 10.4.1)

Cytotoxicity *in vitro*

In vitro cytotoxicity of BPDC NCs were evaluated using both HeLa cells and 4T1 cells. Briefly, cells were initially seeded in a 96-well cell culture plate (5×10^3 cells per well) at

View Article Online
DOI: 10.1039/C9BM00351G

37 °C overnight. Afterwards, free DOX, free Ce6, Bi_2Se_3@PEG NCs or BPDC NCs dispersed in DMEM at various concentrations were introduced to replace the previous medium. After incubation for 4h, the cells were exposed to the 808nm laser ($2W \cdot cm^{-2}$) for 5 min and the 660 nm laser ($0.38\ W \cdot cm^{-2}$) for another 5 min. After following 24h incubation, cell viability in each well was measured in accordance with standard MTT cell viability assay using abovementioned Equation (3).

Hemolysis assay

Mouse whole blood was firstly collected from orbital venous plexus by retro-orbital puncture. Next, red blood cells (RBCs) were isolated through the centrifugation of whole blood at 3000 rpm for 5 min, followed by washing four times with 1×PBS. To carry out the hemolysis test, 0.5 mL of RBCs (4%, v/v) was mixed with 0.5mL of 1×PBS containing Bi_2Se_3@PEG NCs at different concentrations (40, 100, 200 and 400 $\mu g \cdot mL^{-1}$), and incubated at 37 °C for 8 h. RBCs loaded in DI water and 1×PBS were set as the positive and negative control groups, respectively. Thereafter, all the samples were centrifuged at 12,000 rpm for 10 min, and optical absorbance of the supernatants at 570 nm was measured using a UV-vis spectrophotometer (Shimadzu UV-1800, Japan).

Establishment of tumor models

All animal procedures were performed in accordance with the Guide for Care and Use of Laboratory Animals of Southwest University and the experiments were approved by the Institutional Animal Care and Use Committee (IACUC) of Southwest University. Female

View Article Online
DOI: 10.1039/C9BM00351G

BALB/c mice (4-6 weeks of age, 22~25 g each) was subcutaneously inoculated with 4T1 cells (1×10^6 in saline) on dorsal side. Then, all the mice were raised and housed in animal house for ~10 days till the tumor volume reached 150~200 mm^3. The tumor volume was dynamically recorded post-injection and calculated based on Equation (4).

$$\text{Tumor volume} = (\text{Tumor length}) \times (\text{Tumor width})^2 \times 0.5 \quad (4)$$

where length represents the longest dimension and width is taken as the shortest dimension of a tumor.

Pharmacokinetics and biodistribution

To investigate the blood circulation of BPDC NPs, healthy KM mice were intravenously administered with 200 μL of free DOX or BPDC NPs (equivalent DOX dosage: 4 $mg\cdot kg^{-1}$) through the tail vein. At predesignated time points, fresh blood was collected from orbital venous plexus by retro-orbital puncture. 50 μL of blood was dissolved in 250 μL of PBS, which was further treated by a centrifugation at 3000 rpm for 10 min. Then, DOX content in the supernatant was determined based on fluorescence spectrometry through a microplate reader (SPARK 10M, Tecan). To evaluate the biodistribution of BPDC NCs or DOX, female BALB/c mice bearing 4T1 tumors were injected with BPDC NCs or DOX (equivalent DOX dosage: 4 $mg\cdot kg^{-1}$) through caudal vein. At 24 h post-administration, the mice were sacrificed to collect the major organs and tumors. The tissues were weighed and homogenized in DMSO, followed by centrifugation at 13400 rpm for 10 min. Finally, DOX content in supernatant was determined based on fluorescence spectrometry.

View Article Online
DOI: 10.1039/C9BM00351G

Fluorescence/CT imaging property

For fluorescence imaging *in vivo*, BALB/c mice bearing 4T1 tumors were intravenously injected with BPDC NCs (equivalent DOX concentration: 4 $mg \cdot kg^{-1}$). At predesigned time points, infrared fluorescence images of mice were acquired using a fluorescence imaging system (Fusion FX7 Spectra, VILBER, France). The mice were sacrificed at 24 h post-injection, and tumors as well as major organs were excised for *ex vivo* imaging. To evaluate the CT imaging properties, BPDC NC dispersion (in 1×PBS) at various concentrations (1.25, 5, 20, 30 $mg \cdot mL^{-1}$) were loaded in centrifuge tubes and tested through an in-vivo microCT (vivaCT 40).

***In vivo* antitumor effect and biosafety of BPDC NCs**

The previously established 4T1 tumor model was randomly divided into six groups: group 1 (saline), group 2 (BPDC NCs), group 3 (Bi_2Se_3@PEG NCs plus laser), group 4 (free DOX), group 5 (free Ce6 plus laser), and group 6 (BPDC NCs plus laser). 200 μL of liquid sample (equivalent DOX dosage: 4 $mg \cdot kg^{-1}$) was intravenously injected into the tail vein. At 24 h post-injection, the tumor region of mice was illuminated by an 808 nm laser (1.5 $W \cdot cm^{-2}$) for 5 min and a 660 nm laser (0.38 $W \cdot cm^{-2}$) for 5 min in sequence for group 3, 4 and 6. An IR thermal camera (Fluke, TiS55) was used to record the local temperature change of the tumor region. After the treatments, tumor volume and mouse body weight were dynamically measured for 14 days. Then, all the mice were sacrificed and vital organs as well as tumors were collected for hematoxylin and eosin (H&E) and

View Article Online
DOI: 10.1039/C9BM00351G

terminal deoxynucleotidyl transferase dUTP nick end labeling (TUNEL) staining. Optical microscopic images of the histological section were taken under a fluorescence microscope (IX73, Olympus, Japan). The tumor growth inhibition (TGI) index was calculated according to equation (5).

$$TGI = (V_C - V_T)/V_c \times 100\% \quad (5)$$

where V_C denotes the tumor volume of the saline group, and V_T represents the tumor volume after treatments.

Statistical analysis

Statistical analyses complied with one-way analysis of variance (ANOVA) and were performed using OriginPro 9.0 (OriginLab, MA, USA). A *p*-value less than 0.05 (*p<0.05, n = 4) was considered to be the minimal level of significance.

Results and discussion

Synthesis and characterizations of BPDC NCs

The synthesis procedures of BPDC NCs is schematically illustrated as Fig. 1. Bi_2O_3 NPs were firstly synthesized based on a solvothermal method. Then, Bi_2Se_3 NCs were subsequently obtained after a simple hydrothermal process by using the as-developed Bi_2O_3 NPs as the precursor and template incorporation with ascorbic acid and sodium selenite. After the surface modification with PEG, antitumor drug of DOX and photosensitizer Ce6 were loaded into hollow Bi_2Se_3 NCs via hydrophobic action and

View Article Online
DOI: 10.1039/C9BM00351G

electrostatic adsorption. FESEM image showed that as-synthesized Bi_2O_3 NPs displayed spherical morphology and the hydrodynamic size was measured as ~183.7 nm using DLS (Fig. S1a, S2a). In addition, high-resolution TEM image indicated their highly porous structure (Fig. 2a). Bi_2Se_3 NCs prepared from Bi_2O_3 NPs also exhibited spherical structure and were uniformly distributed (Fig. S1b). Excitingly, TEM result revealed a highly porous and hollow nanostructure of Bi_2Se_3 NCs, and the hydrodynamic size was measured as ~181.6 nm from DLS analysis (Fig. 2b, S2b). The porosity of Bi_2O_3 NPs, Bi_2Se_3 NCs and BPDC NCs were further investigated via Brunauer–Emmett–Teller (BET) analysis of nitrogen adsorption−desorption isotherms. The BET surface area and total pore volume of Bi_2Se_3 NCs are determined as 28.106 $m^2 \cdot g^{-1}$ and 0.162 $cm^3 \cdot g^{-1}$, respectively. Therefore, the pore size of Bi_2Se_3 NCs was calculated as 4.35 nm, which was slightly larger than that of Bi_2O_3 NPs as 3.26 nm (Fig. 2d-e, S3a-b). These results clearly confirmed the hollow mesoporous structure of Bi_2Se_3 NCs, benefiting in the encapsulation of therapeutic molecules with high loading content. Compared to Bi_2Se_3 NCs, the average pore size of BPDC NCs decreased to 3.46 nm, which can be explained as the mild pore blockage from PEGylation and drug loading (Figure S3c-d). Moreover, the region indicating BPDC NC cavity became more darkened as observed from TEM imaging, indicative of a successful drug encapsulation (Fig. 2c). Crystal structures of all the intermediate and final products are characterized by X-ray diffraction (XRD). XRD pattern of Bi_2O_3 NPs displayed a low crystallinity and was consistent with the JCPDS card (No. 76-0147) of standard bismuth oxide (Fig. S4a). Moreover, all the diffraction peaks in the XRD pattern of Bi_2Se_3 NCs can be precisely indexed to the JCPDS card (No. 12-0732), implying the presence of Bi_2Se_3 nanocrystal in the sample (Fig. 2f). The

View Article Online
DOI: 10.1039/C9BM00351G

valence states and chemical composition of Bi_2O_3 NPs and Bi_2Se_3 NCs were further analyzed through XPS and Energy-dispersive X-ray spectroscopy (EDS). The XPS spectrum of Bi_2O_3 NPs demonstrated the coexistence of Bi and O elements, verifying the successful synthesis of pure Bi_2O_3 NPs (Fig. S4b-d). Similarly, strong Bi and Se signals in the XPS survey spectrum manifested the co-existence of Bi and Se atoms in as-developed Bi_2Se_3 NCs (Fig. 2g). The signals of oxygen and carbon were presented owing to the oxygen adsorption on the surface of NCs and the carbon film for sample loading. High-resolution XPS spectrum displayed two characteristic peaks at 164.5 eV and 159.3 eV, assigned to Bi $4f_{7/2}$ and Bi $4f_{5/2}$ of Bi_2Se_3 NCs, respectively (Fig. 2h). Moreover, core level XPS spectrum of Se3d exhibited two characteristic peaks at 53.3 eV (Se $3d_{5/2}$) and 54.1eV (Se $3d_{3/2}$) as shown in Fig. 2i. The chemical composition of the samples was further analyzed by means of EDS linear scanning analysis under FESEM. Intense peaks corresponding to Bi and Se were detected in Bi_2Se_3 NCs (Fig. 3a-d), and peaks representing Bi and O were observed in Bi_2O_3 NPs (Fig. S5). The XPS and EDS results strongly evidenced the successful synthesis of Bi_2O_3 NPs and Bi_2Se_3 NCs.

View Article Online
DOI: 10.1039/C9BM00351G

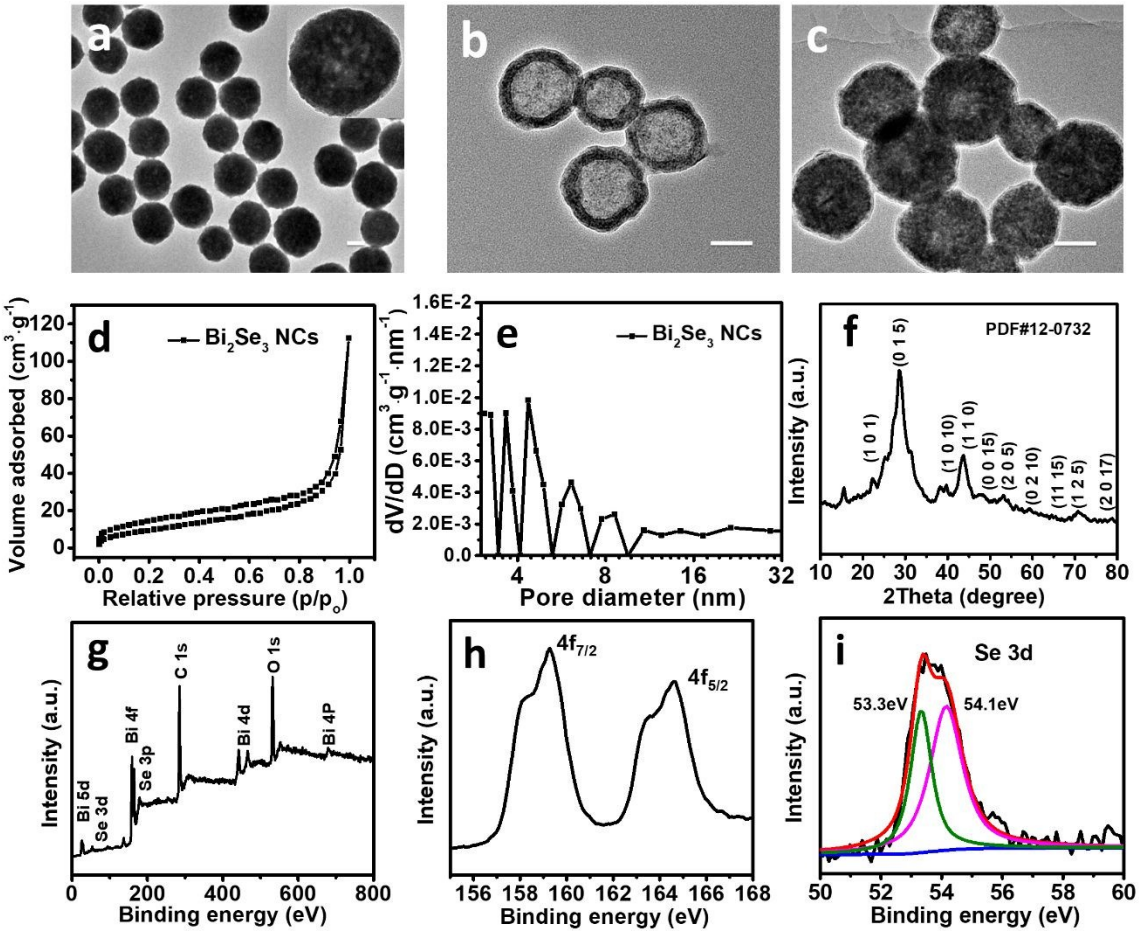

Fig. 2. TEM images of (a) Bi_2O_3 NPs, (b) Bi_2Se_3 NCs and (c) BPDC NCs (scale bars: 50 nm); (d) N_2 adsorption–desorption isotherm and (e) the corresponding pore size distribution of the Bi_2Se_3 NCs; (f) XRD spectrum of Bi_2Se_3 NPs; (g-i) XPS characterization of Bi_2Se_3 NCs: (g) the survey of full spectrum and core level spectrum of (h) Bi4f (i) Se3d.

The hydrodynamic diameter of Bi_2Se_3@PEG NCs and BPDC NCs was measured as 212.5 and 215.2 nm, respectively (Fig. 3e, S2c). Moreover, there was no obvious change in the hydrated particle size during the incubation for seven days, suggesting a good stability of BPDC NCs under aqueous condition (Fig. S2d). Zeta potential of Bi_2Se_3@PEG NCs and BPDC NCs were respectively recorded as 35.6 mV and 31.6 mV

View Article Online
DOI: 10.1039/C9BM00351G

(Fig. 3f), and the negative surface potential may potentially extend their circulation half-life in blood[2]. FT-IR spectrum of the key components (DOX, Ce6, PEG-SH, Bi_2Se_3 NCs, and BPDC NCs) were measured to confirm the composition of final products (Fig. S6a, b). Typical peaks of DOX were presented at 3450 cm^{-1} and 3325 cm^{-1}, ascribed to the stretching vibrations of N-H and O-H groups, respectively.[43] The stretching vibration of C-H and C-O groups from Ce6 were donated by the peak at 2890 cm^{-1} and the broad band in the region of 1100-1300 cm^{-1}.[44] The peaks at ~2870 and ~3440 cm^{-1} of SH-PEG indicated typical C-H and O-H bond stretching vibrations, respectively.[45] As expected, BPDC NCs exhibited the major characteristic peaks of all the building blocks by analysing the FT-IR spectrum, verifying a rational design and successful synthesis. The weight proportions of Bi_2Se_3 and PEG in the Bi_2Se_3@PEG NCs were calculated as 89.6% and 10.4% based on TGA, respectively, manifesting an effective conjugation of PEG onto Bi_2Se_3 NCs (Fig. S6c). The fluorescence spectra of BPDC NCs exhibited a concurrent presence of the characteristic emission peaks of DOX and Ce6 at 560 nm and 660 nm, respectively, suggesting the successful loading of both therapeutic molecules (Fig. 4a). The fluorescence intensity for both DOX and Ce6 slightly decreased after loading into the NCs, which can be explained as the self-quenching of fluorescence owing to their existence in an aggregated state.[46, 47] The UV-vis-NIR spectrum of BPDC NCs displayed three characteristic absorption peaks at ~405nm, ~660 nm and ~480 nm, which can be further interpreted as the effective loading of Ce6 and DOX (Fig. 4b). The resultant BPDC NCs possessed strong light-absorbing in NIR region and the absorbance at 808nm was positively correlated with the sample concentration, implying a good potential of applying BPDC NCs as photothermal agents for PTT (Fig. 4c, S7a).

View Article Online
DOI: 10.1039/C9BM00351G

Excitingly, BPDC NCs can be well dispersed in DI water, PBS and DMEM, and no obvious aggregation was observed within 8 h incubation, verifying their acceptable stability and dispersity for clinical applications (Fig. S7b).

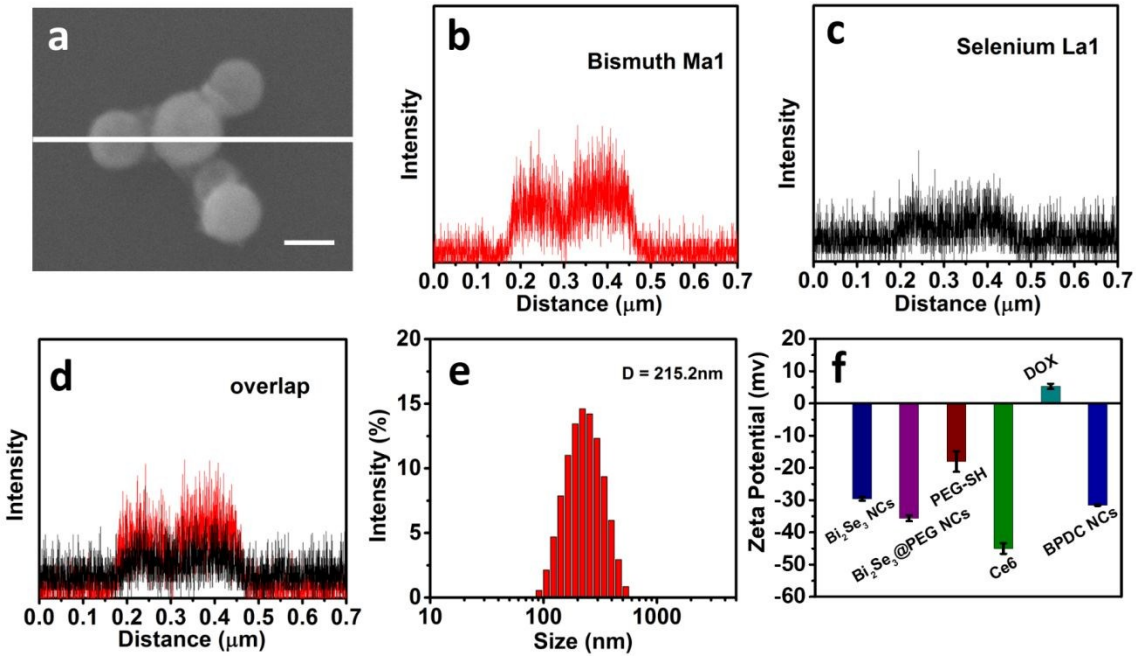

Fig. 3. (a) Typical TEM image of Bi_2Se_3 NCs (scale bar: 100 nm); (b-d) linear scanning results of the cross-section of individual Bi_2Se_3 NC based on EDS analysis; (e) size distribution of BPDC NCs characterized by DLS; (f) Zeta potentials of Bi_2Se_3 NCs, Bi_2Se_3@PEG NCs, PEG-SH, Ce6, DOX and BPDC NCs.

Photothermal behavior of BPDC NCs *in vitro*

The photothermal properties of Bi_2Se_3 NCs and BPDC NCs were further monitored by exposing the sample-laden cuvette (100 μg·mL^{-1}) to NIR laser (808 nm, 2 W·cm^{-2}). Temperature of the aqueous dispersion of Bi_2Se_3 NCs and BPDC NCs increased to 59.7 °C and 56.3°C within 10 min NIR irradiation, in sharp contrast to 26.6°C of DI

View Article Online
DOI: 10.1039/C9BM00351G

water (Fig. 4d). Moreover, temperature elevation rate of BPDC NCs was positively correlated to the sample concentration ranging from 20 to 100 μg·mL^{-1} (Fig. 4e, S8a). Particularly, the system temperature containing BPDC NCs can be elevated to 45.6 °C at a relatively low concentration of 60 μg·mL^{-1} upon 10 min exposure to NIR light, which exceeded the threshold temperature of 43^{o}C for tumor ablation.[48] Meanwhile, temperature increase of BPDC NCs also exhibited a NIR laser power dependent manner (Fig. S8b-c). The high thermal contrast produced by the BPDC NC suspensions was further proved by the thermographic imaging, and the results were in line with the data obtained using digital thermometer (Fig. 4g-h). Therefore, photothermal performance of BPDC NCs was expected to be adjustable by customizing the sample concentration, laser output power and laser irradiation time. The photothermal conversion stability of BPDC NCs (100 μg·mL^{-1}) was investigated by consecutive NIR laser irradiations for four cycles (Figure 4f). There was no obvious change in the peak temperature of all irradiation cycles, indicating a good photothermal conversion stability of BPDC NCs. In addition, the photothermal conversion efficiency (η) of BPDC NCs was identified as 32.3% (Figure S9), which is comparable to Bi_2Se_3 nanoplate (34.7%) [49] and is considerably higher than the currently extensively studied photothermal agents including gold nanorods (21%),[50] CuS NPs (25.7%),[51] and MoS2 (24.37%).[52] The strong and broadband NIR absorbance, infrared thermal imaging capacity, and high photothermal conversion efficiency as well as stability render the BPDC NCs as a highly promising PTT nanoagent.

View Article Online
DOI: 10.1039/C9BM00351G

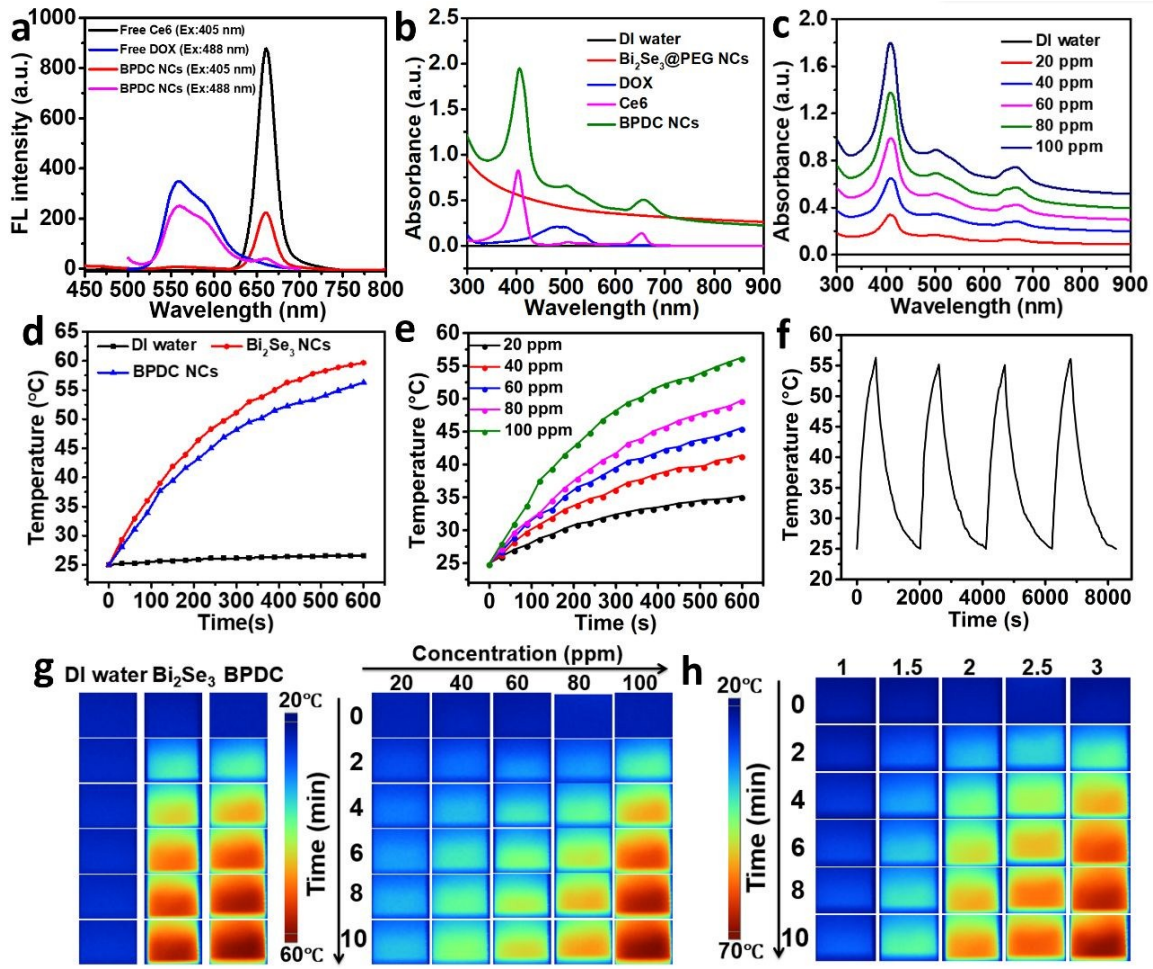

Fig. 4. (a) Fluorescence spectra of Ce6, DOX and BPDC NC aqueous dispersion (equivalent DOX concentration: 5 μg·mL^{-1}) under various excitation wavelength; (b) optical absorption spectra of Bi_2Se_3@PEG NCs, Ce6, DOX and BPDC NCs through UV-vis-NIR spectroscopy; (c) absorption spectra of BPDC NC aqueous dispersion at various concentrations through UV-vis-NIR spectroscopy; (d) temperature elevation of the aqueous dispersions of BPDC NCs (100 ppm) , Bi_2Se_3 NCs (100 ppm) and DI water under NIR laser irradiation for 10 min; (e) temperature elevation of the BPDC NC dispersions at gradient concentrations (0 to 100 ppm) under NIR laser irradiation for 10 min; (f) temperature change of BPDC NC aqueous dispersion (100 ppm) under cyclic laser illuminations; (g) thermographic images of the sample-laden cuvettes corresponding

View Article Online
DOI: 10.1039/C9BM00351G

to (d) and (e); (h) thermographic images of the sample-laden cuvettes corresponding to Fig. S8b.

***In vitro* stimuli-responsive drug release**

Highly mesoporous and hollow structure of Bi_2Se_3 NCs allows the effective encapsulation of small molecule therapeutic agents, such as DOX and Ce6. As expected, the DLC for Ce6 and DOX were determined as high as 11.9% and 18.1%, respectively. And, the corresponding EE for Ce6 and DOX were determined as 13.6% and 20.1%, respectively. To validate the controlled drug release property of BPDC NCs, pharmacokinetics of DOX release was monitored under different pH values and thermal shock activated by NIR laser irradiation. As shown in Fig. S10a, 45.6% and 26.9% of DOX was respectively released from BPDC NCs at pH=5.0 and 6.5 during 24 h incubation, in markedly contrast to that of 17.7% in neutral condition (pH=7.4). The protonation of amino group of DOX under acidic condition can enhance drug hydrophilicity and decrease drug binding affinity, resulting in the drug release from the nanocarriers.[53] Given the acidic tumor microenvironment, BPDC NCs are ought to be advantageous for tumor-specific drug delivery. In addition, NIR-responsive drug release was assessed through periodic on/off NIR laser irradiation (laser on for 5 min per cycle). Distinctly, accelerated drug release was observed during laser irradiation period under all pH conditions (Fig. S10b). During 24 h incubation with six laser irradiation cycles, cumulative drug release can reach up to 44.3%, 59.1% and 83.1% under pH 7.4, 6,5 and 5.0, respectively, which were immensely higher than those obtained under dark condition. Referring to previous reports, NIR-light induced local hyperthermia may disrupt the

View Article Online
DOI: 10.1039/C9BM00351G

binding between DOX and nanocarrier and further increase the drug diffusion rate.[54, 55] Therefore, these findings explicitly indicate that BPDC NCs may potentially realize tumor-specific drug delivery, and drug release rate could be adjustable upon NIR laser irradiation.

Cellular uptake and internalization

The effective cellular uptake of therapeutic molecules mediated by BPDC NCs is a prerequisite for exerting their theranostic functions. Herein, intracellular internalization of BPDC NCs were explored by using HeLa cells and 4T1 cells. As illustrated in confocal imaging of Fig. 5a, the fluorescence signals of both Ce6 and DOX intensified with the incubation time from 1 h to 4 h, indicating an effective drug internalization mediated by BPDC NCs. Particularly, Ce6 signal was primarily distributed in the region of cytoplasm, favoring the PDT effect that targets the organelles. Differently, DOX signal can be observed both in the nuclei and cytoplasm, attributed to the partial release of DOX from BPDC NCs. Flow cytometry was further conducted to quantify the cells that took in a significant amount of DOX, which was confirmed by a distinctly upgraded fluorescence level as compared to blank controls. A clear shift of peak fluorescence intensity toward high energy levels was observed with the increase of incubation time, validating the cellular uptake of DOX by HeLa cells (Fig. 5b, c). More specifically, the percentage of cells intake of a significant amount of DOX increased from 37.75% at 0.5 h to 96.26% at 6 h, implying a rapid cellular internalization mediated by BPDC NCs (Fig. 5d). Similar results were also revealed by examining the 4T1 cells (Fig. S11).

View Article Online
DOI: 10.1039/C9BM00351G

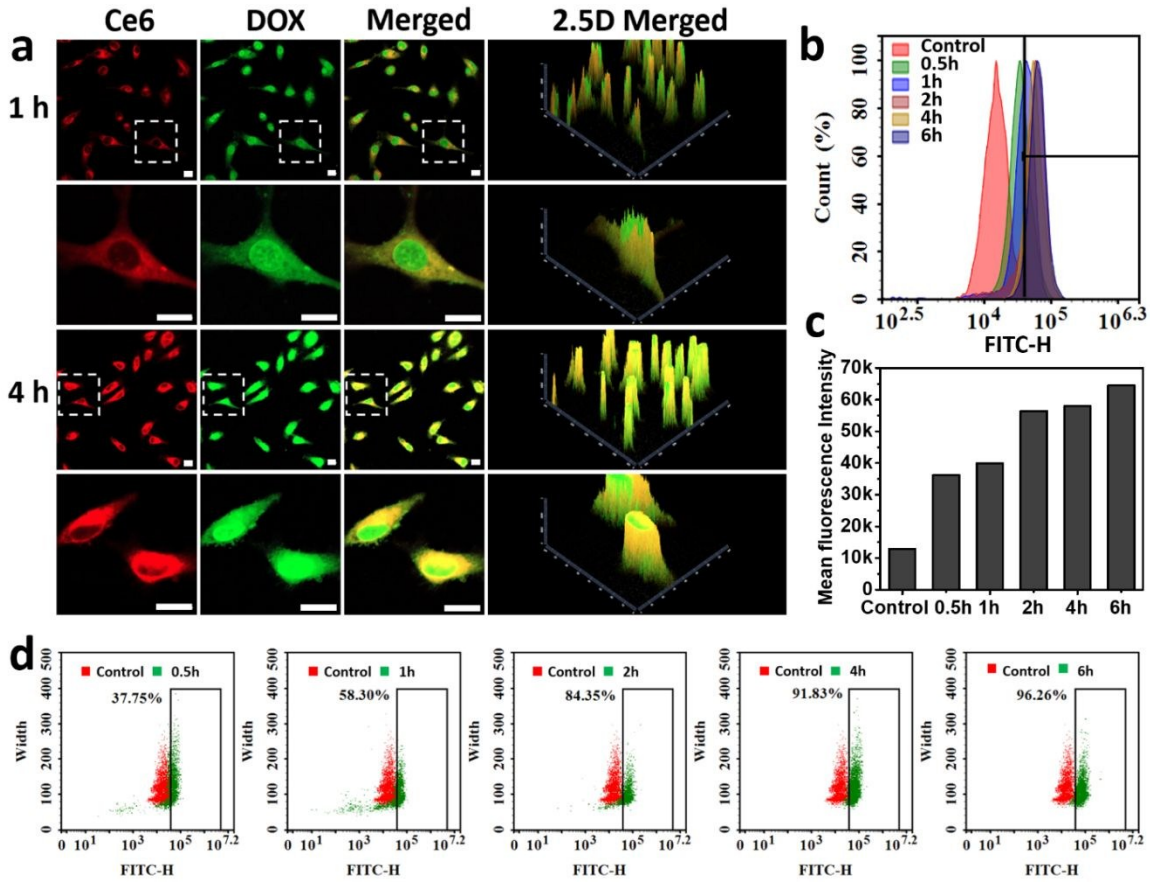

Fig. 5. Evaluation of cellular uptake of DOX mediated by BPDC NCs. (a) Confocal microscopy: fluorescence imaging of HeLa cells after being treated by BPDC NCs for 1 h or 4 h (scale bars: 20 μm). Green and red color represent the fluorescence emission of DOX and Ce6, respectively (Images of 2nd and 4th row are the magnification of dashed box enclosed area in 1st and 3rd row, respectively); (b) flow cytometry to analyze the cellular uptake of DOX mediated by BPDC NCs in HeLa cells after various treatment periods; (c) mean intensity of DOX fluorescence emission from cells corresponding to (b); (d) flow cytometry dot plots of HeLa cells after being treated by BPDC NCs for different periods.

View Article Online
DOI: 10.1039/C9BM00351G

Intracellular generation of ROS

Reactive oxygen species (ROS) plays an important role in cell survival, death, differentiation and cell signalling, and are fundamental for photodynamic therapy (PDT). Light-mediated ROS generation is the main cause underlying the efficacy of photodynamic therapy. In this study, the yield of intracellular ROS was evaluated *in vitro*, by using an active oxygen probe of DCFH-DA. This probe can be hydrolysed into DCFH intracellularly, and two-electron oxidation of DCFH results in the formation of a fluorescent product of dichlorofluorescein (DCF). Because of the overlapped fluorescence emission spectra of DCF and DOX, DOX excluded Bi_2Se_3@PEG/Ce6 (BPC) NCs were investigated to eliminate the interference during ROS detection, and free Ce6 was concurrently investigated for comparison. As shown in Fig. 6, fluorescence in DCF channel cannot be observed in the HeLa cells treated with Ce6 or BPC NCs in the absence of 660 nm laser irradiation, suggesting a negligible presence of intracellular ROS. In contrast, vivid green fluorescence can be found in the Ce6 or BPC NCs treated cells under 660 nm laser irradiation, manifesting a prominent ROS generation. Compared to the cells treated by free Ce6, notable amount of ROS yield was found in the cells treated by BPC NCs as evidenced by the stronger green fluorescence emission in DCF channel, which could be interpreted as the enhanced cellular uptake of Ce6 mediated by the nanocarriers. Similarly, BPC NCs also produced remarkable ROS in 4T1 cell line upon laser irradiation (Fig. S12). These results demonstrated that BPC NCs may serve as the potent nanocarriers for more efficient intracellular delivery of Ce6, resulting in a higher light-activated ROS yield.

View Article Online
DOI: 10.1039/C9BM00351G

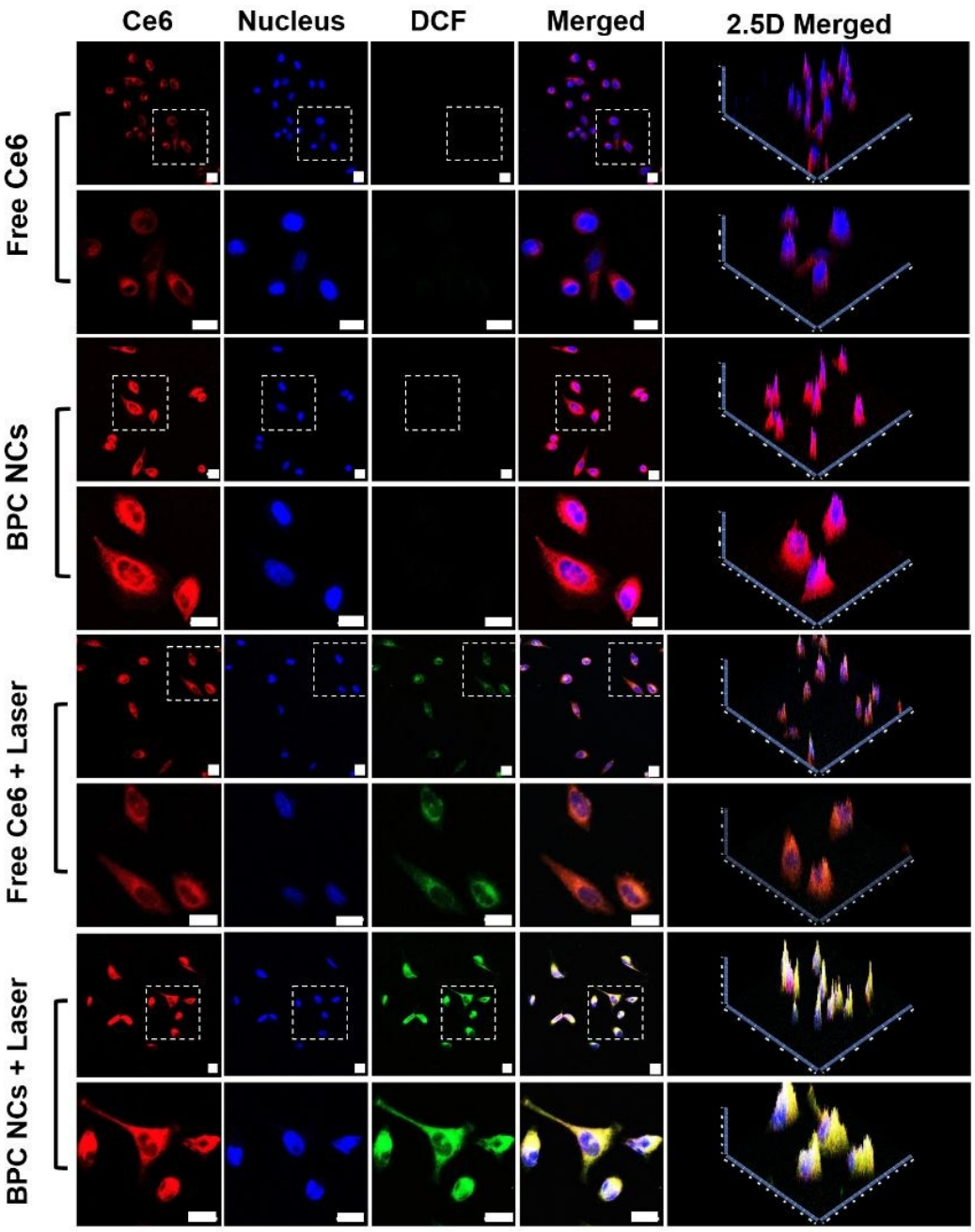

Fig. 6. Characterization of intracellular ROS production using DCFH-DA probe: confocal imaging of HeLa cells being treated with free Ce6 or BPC NCs subject to 660 nm laser irradiation where applicable (scale bars: 20 μm). Images in 2nd, 4th, 6th and 8th rows display the magnified areas enclosed in dashed box in 1st, 3rd, 5th and 7th rows, respectively.

View Article Online
DOI: 10.1039/C9BM00351G

PTT/PDT-induced cell ablation in vitro

Mitochondria play key roles in activating apoptosis in tumor cells.[56] Oxidative stress caused by excessive ROS and local hyperthermia shock may result in the mitochondrial dysfunction.[57] Mitochondrial membrane potential (MMP) is a central parameter to indicate the physiological and pathological conditions of mitochondria and can be evaluated through JC-1 fluorescence staining kit. JC-1 accumulates in mitochondria, and selectively assembles into J-aggregates to produce orange fluorescence (emission peak: 590 nm) in normal cells. However, these aggregates may leak out from the mitochondria to the cytosol as monomers in apoptotic cells, which emit green fluorescence (emission peak: 520 nm). Thus, we examined the apoptosis of HeLa cells induced by BPC NCs and other intermediate products subject to laser irradiation (Fig. S13). Similar with the untreated group, only orange fluorescence can be observed in the cells with the treatment by BPC NCs or laser irradiation, suggesting a resting state of mitochondria without mitochondrial depolarization. In the meanwhile, weak green fluorescence representing the generation of JC-1 monomers in the cells with the treatment by Bi_2Se_3@PEG NCs or Ce6 under laser irradiation, manifesting a slight mitochondrial damage caused by PDT or PTT, respectively. Astoundingly, vivid green fluorescence was found in the cells administrated by BPC NCs upon laser irradiation, indicating a markedly cellular apoptosis induced by combined PTT/PDT. Similar results were also observed when examining the 4T1 tumor cells *in vitro* (Fig. S14).

View Article Online
DOI: 10.1039/C9BM00351G

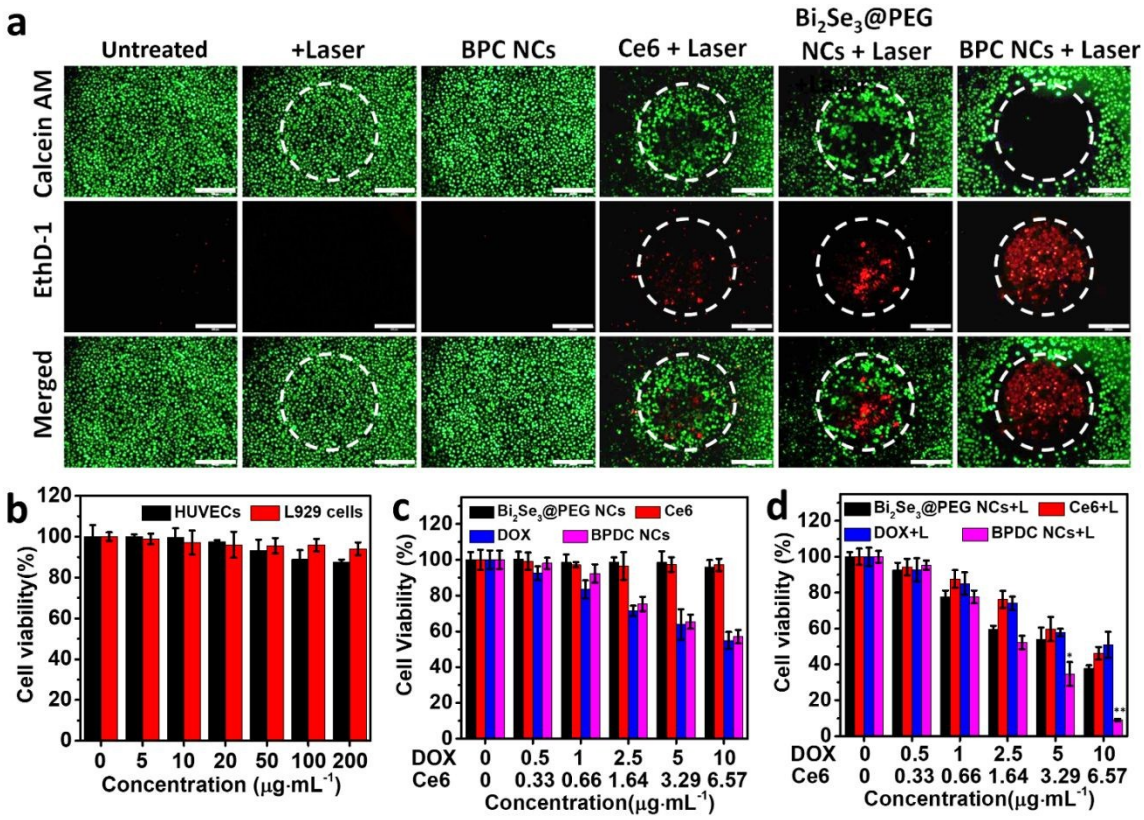

Fig. 7. (a) Fluorescence images of HeLa cells stained by Live/Dead cell viability assays after different treatments. The dashed circles represent irradiated spot (scale bars: 200 μm). The green and red dots respectively represent the live and dead cells; (b) viability of HUVECs and L929 cells after being incubated with Bi_2Se_3@PEG NCs at multiple concentrations for 24 h (0 to 200 μg·mL^{-1}); viability of HeLa cells after being treated by Bi_2Se_3@PEG NCs, free Ce6, DOX or BPDC NCs (c) without or (d) with laser irradiation (660 nm+808 nm). $^{*}p<0.05$ and $^{**}p<0.01$ when compared to control groups.

To further verify BPC NCs-mediated PTT/PDT effect, viability of HeLa cells after various treatments was examined using LIVE/DEAD cell staining kit (Fig. 7a). No observable red fluorescence can be found in the groups of unitary BPC NCs or laser irradiation in comparison to the untreated group, suggesting a negligible cell destruction effect. Differently, a mild tumor ablation effect emerged in the cells subject to

View Article Online
DOI: 10.1039/C9BM00351G

Bi_2Se_3@PEG NCs or Ce6 under laser irradiation as indicated by local red fluorescence within the irradiation spot, attributed to the PTT- or PDT-induced cell destruction, respectively. Distinctly, much stronger red fluorescence was observed in the cells treated with BPC NCs under laser irradiation, suggesting a severer cell killing effect arising from a combinatorial PTT/PDT effect. Biocompatibility assessment is essential to support the development and marketing of the biomedical nanoplatform. Thus, the cytotoxicity of Bi_2Se_3@PEG NCs toward HUVECs and L929 cells was evaluated using the standard MTT cell viability assay and LIVE/DEAD cells viability assays (Fig. 7b, S15). The cell viability still exceeded 80% when cells being treated by Bi_2Se_3@PEG NCs at a considerably high concentration of 200 $\mu g \cdot mL^{-1}$, indicating a minimal cytotoxicity and acceptable biocompatibility as drug carriers.

***In vitro* cytotoxicity**

BPDC NCs-mediated tumor cell destruction from combined PTT/PDT/chemotherapy was explored on HeLa cells after multiple treatments through MTT assays (Fig. 7c, d). Negligible cell death was confirmed in the cells treated by Bi_2Se_3@PEG NCs or free Ce6, indicating a weak dark toxicity. In contrast, much lower cell survival rates were revealed in the cells being incubated with free DOX or BPDC NCs, particularly at the equivalent DOX concentration higher than 1 $\mu g \cdot mL^{-1}$, attributed to the underlying chemotherapeutic effect (Fig. 7c). When applying laser irradiation, prominent cytotoxicity was found in the groups of Bi_2Se_3@PEG NCs and Ce6 at higher drug concentrations, owing to the markedly PTT and PDT effects, respectively (Fig. 7d). Distinctly, the most remarkable tumor cell damage occurred in the group of BPDC NCs plus laser irradiation, manifesting

View Article Online
DOI: 10.1039/C9BM00351G

a combined PTT/PDT/chemotherapy effect. The cell killing efficacy was enhanced with the increase of agent concentrations, and cell viability rapidly decreased to ~8.79% at an equivalent DOX concentration of 10 $\mu g \cdot mL^{-1}$. These data corresponded well with the previous findings in Live/Dead cell staining (Fig. 7a). In another aspect, 4T1 tumor cells showed similar responses to the same treatment recipes (Fig. S16). Moreover, BPDC NCs also imposed an unavoidable dark toxicity toward HUVECs and L929s in the absence of laser irradiation, which was comparable with the findings in HeLa and 4T1 cells (Fig. S17). Therefore, all these results revealed that BPDC NCs can serve as a potent and advantageous platform to achieve multimodal tumor therapy.

Pharmacokinetics and biodistribution

Highly efficient accumulation of nanoagents into tumor region via EPR effect is indispensable for efficacious tumor therapy. Moreover, prolong blood circulation may increase the drug targeting into tumorous tissue. Therefore, pharmacokinetic parameters of BPDC NCs was obtained in KM mice by detecting the DOX content in circulating blood using fluorescence spectrometry (Fig. 8a). At 24 h post-administration, ~8.64 $ID \cdot g^{-1}$ (equivalent DOX dose per gram of tissue) was discovered in peripheral circulating blood, which was immensely higher than ~1.92 $ID \cdot g^{-1}$ of free DOX. The results implied a considerably longer circulation half-life of BPDC NCs, favoring their accumulation in tumor site through passive targeting. Biodistribution of BPDC NCs in BALB/c mice bearing 4T1 tumors was examined by quantifying the DOX content in major organs and tumors at 24 h post-injection (Fig. 8b). Relatively higher retention of BPDC NCs in liver and spleen suggested a typical capture by reticuloendothelial system (RES). Besides, a

View Article Online
DOI: 10.1039/C9BM00351G

notable BPDC content of ~10.1 ID·g^{-1} in excised tumors at 24 h, tremendously higher than ~3.8 ID·g^{-1} of free DOX, manifesting efficient tumor-specific tumor accumulation of BPDC NCs via EPR effect and prolonged blood circulation.

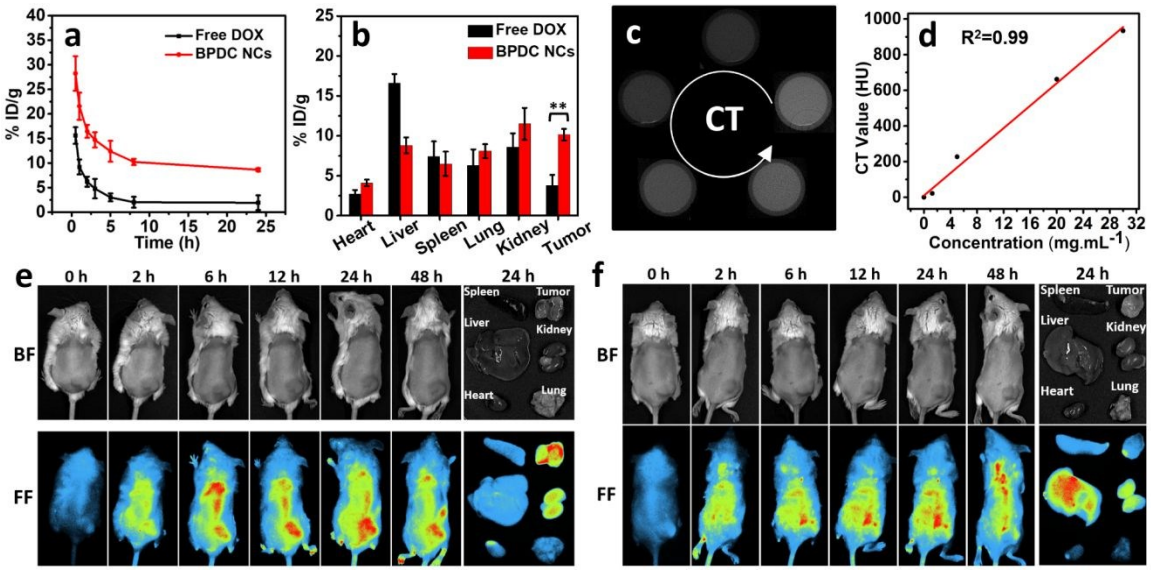

Fig. 8. (a) Pharmacokinetics of BPDC NCs or free DOX over 24 h after intravenous injection to KM mice; (b) biodistribution of BPDC NCs or free DOX at 24 h post-injection to BALB/c mice bearing 4T1 tumors ($^{**}p < 0.01$ between two groups); (c) *in vitro* CT images of BPDC NCs; (d) CT intensity values of BPDC NC aqueous dispersion at different concentrations; fluorescence images of BALB/c mice bearing 4T1 tumors before and after the administration of (e) BPDC NCs and (f) Ce6. Major organs and tumors were excised from both groups at 24 h post-injection.

In vivo antitumor effect and biosafety of BPDC NCs

The CT imaging property of BPDC NCs was examined by taking the phantom photos of their aqueous dispersion at different concentrations *in vitro* (Fig. 8c-d). It was worth noting that the brightness of CT phantom photos progressively intensified with the rising

View Article Online
DOI: 10.1039/C9BM00351G

concentrations of BPDC NCs, implying an opportunity of applying BPDC NCs as CT contrast agents. An X-ray absorption coefficient of 31.51 HU·mL·mg^{-1} was derived from the linear equation of fitted curve (Fig. 8d), which was dramatically higher than that of iopromide (16.4 HU·mL·mg $^{-1}$), deemed as a widely-used commercial CT contrast agent for clinics.[58, 59] Ascribed to the intrinsic fluorescence property of Ce6, the fluorescence imaging capacity of BPDC NCs was studied in BALB/c mice bearing 4T1 tumors upon intravenous injection (Fig. 8e). At 24 h post-injection, effective accumulation and enrichment of BPDC NCs was found in solid tumor region, as evidenced by the strong local fluorescence emission, which was in line with biodistribution results (Fig. 8b). The ex-vivo imaging of tumors and major organs further confirmed higher tumor uptake and retention of BPDC NCs because of their prolonged blood circulation than free Ce6 (Fig. 8e-f). Therefore, the pronounced fluorescence and CT imaging properties of BPDC NCs could validate the potentially multimodal imaging for improved cancer diagnosis and prognosis.

The antitumor efficacy of BPDC NCs was subsequently evaluated using a 4T1 tumor xenografted BALB/c mouse model. The tumor-bearing mice were randomly divided into six groups for administration when the tumor volume reached 200 mm^3. The thermal response of tumor region at 24 h post-injection was firstly investigated utilizing an infrared thermal camera upon NIR laser irradiation (Fig. 9a, b). In comparison to the control groups, temperature of tumor region in the mice treated by Bi_2Se_3@PEG NCs and BPDC NCs promptly increased to 58.1°C and 57.9 °C upon 5 min NIR laser irradiation, revealing a superior photothermal response. Afterwards, the antitumor effect mediated by BPDC NCs was explored by monitoring the tumor volume change within 14 day after

View Article Online
DOI: 10.1039/C9BM00351G

various treatment (Fig. 9d). The fastest tumor growth was observed in saline group. Differently, groups of 3, 4 and 5 exhibited a limited level of tumor inhibition dependent on the respective effects of PTT, chemotherapy and PDT. Notably, laser-activated BPDC NCs (group 6) induced an extremely high level of tumor suppression with a TGI of 98.79% without any recurrence. Conversely, BPDC NCs can only result in a TGI of 15.8% in the absence of laser irradiation. At day 14 post-administration, the mice were sacrificed to excise the tumors for weighing (Fig. 9c, e). As expected, tumors of the mice in group 6 were the smallest or even disappeared among all the groups, which was consistent with the as-measured tumor volume *in vivo* (Fig. 9d). It was worth noting that the weight of mice was not obviously altered during all the treatments, attesting the minimal systemic toxicity and side effects (Fig. 9f). Finally, the excised tumors were histologically examined by H&E staining and TUNEL assay. H&E staining indicated a regular morphology of tumor cells with intact nuclei in group 1 treated by saline. In comparison to groups 2-5, the most severe nucleus damage were observed in the tumoral tissues of the mice treated with laser-activated BPDC NCs (group 6), implying a prominent tumor cell necrosis (Fig. 9g). In another aspect, the most serious tumor cells apoptosis was revealed in group 6, as proven by the vivid green fluorescence during TUNEL assay (Fig. 9h). These results demonstrated an impressive therapeutic efficacy for tumor ablation through the combined PTT/PDT/chemotherapy mediated by BPDC NCs.

View Article Online
DOI: 10.1039/C9BM00351G

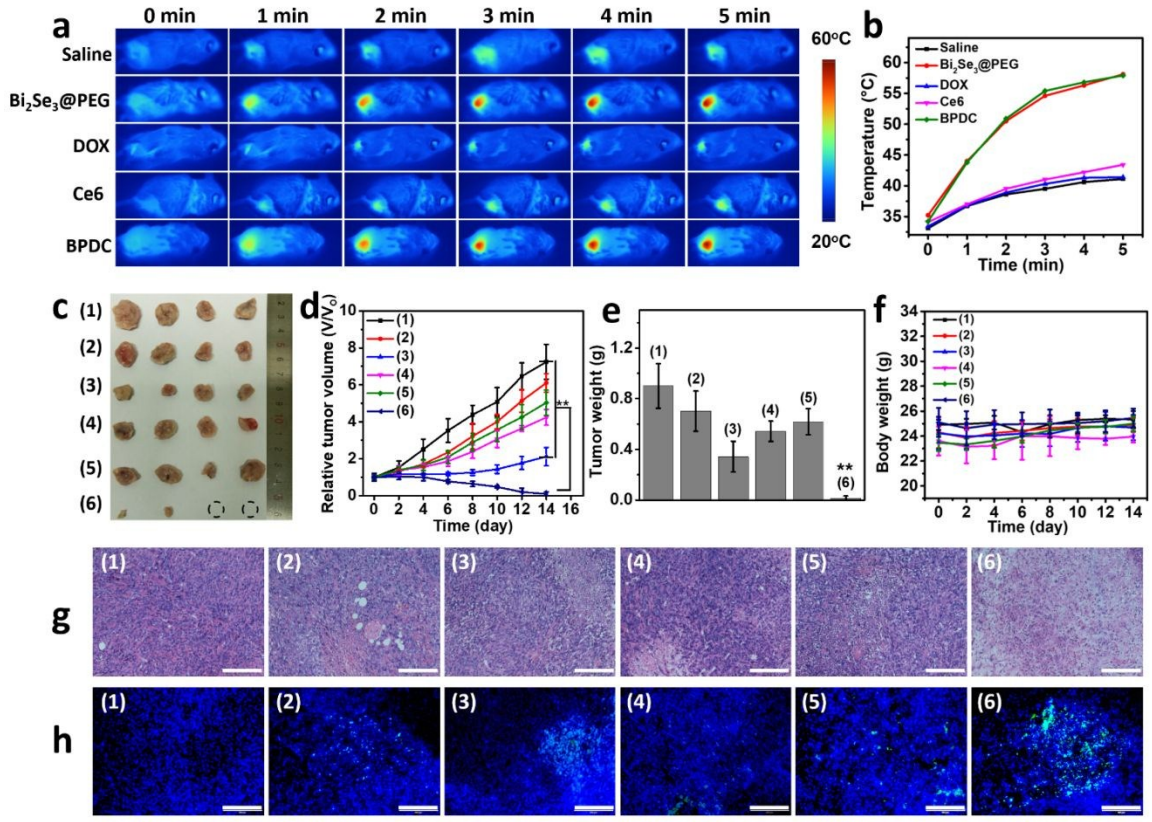

Fig. 9. BPDC NCs induced tumor eradication *in vivo*: (a) infrared thermography of mice after being intravenously injected with diversified agents subject to NIR laser irradiation; (b) local temperature elevation of the tumor sites corresponding to (a); (c) photographs of the tumors excised at day 14 after different treatments; (d) change of tumor volume in 14 days after various treatments ($^{**}p < 0.01$ when compared to control groups); (e) weight of the tumors excised at day 14 after various treatments ($^{**}p < 0.01$ when compared to control groups); (f) change of the mouse weight over 14 days post-administration; histological analysis of tumor sections via (g) H&E staining and (h) TUNEL staining. Group 1 (saline), group 2 (BPDC NCs), group 3 (Bi_2Se_3@PEG NCs plus laser), group 4 (free DOX), group 5 (free Ce6 plus laser), and group 6 (BPDC NCs plus laser).

View Article Online
DOI: 10.1039/C9BM00351G

In addition to the previous assessment of the biocompatibility at the cellular level, we further investigated the biosafety of BPDC NCs through the examination of hemocompatibility and histocompatibility. We firstly explored the Bi_2Se_3@PEG NC-induced hemolytic potential on red blood cells (RBCs). DI water (positive control) is hypotonic to RBCs, which tend to burst and release their content into the surrounding medium, resulting in a complete and irreversible hemolysis. Conversely, 1×PBS (negative control) can mimic an isotonic environment that maintains the integrity of RBC membrane. As displayed in Fig. S18, the maximum hemolysis rate of 3.09% was observed in the RBCs treated by Bi_2Se_3@PEG NCs with a concentration of 200 $\mu g \cdot mL^{-1}$, implying an acceptable hemocompatibility of drug carriers. Furthermore, blood routine test on the peripheral blood was conducted for seven days after the mice were injected with BPDC NCs (Fig. S19, Table S1). All the key blood index fell in the provided reference ranges of healthy mice, suggesting a negligible alternation of blood content after introducing BPDC NCs. Afterwards, major organs of treated mice collected at day 14 was sliced for histological analysis by H&E staining (Fig. S20). No obvious inflammation or lesion was observed at cellular and tissue level in all treated groups. These results explicitly demonstrated a low long-term systemic toxicity of BPDC NCs toward vital organs.

Conclusions

In summary, we have successfully designed and synthesized a multifunctional theranostic agent (BPDC NCs) by loading DOX and Ce6 into PEG-SH decorated hollow mesoporous Bi_2Se_3 NCs, which can be specifically delivered into the tumorous tissue through the EPR

View Article Online
DOI: 10.1039/C9BM00351G

effect as evidenced by the fluorescence imaging. Under the activation in more acidic tumor microenvironment or by exogenous stimulus of laser irradiation, BPDC NCs were responsive to release their encapsulated drugs into the surrounding medium. The significant local hyperthermia and ROS generation mediated by BPDC NCs were simply implemented by composite laser irradiation. As expected, BPDC NCs demonstrated a remarkable anti-tumor effect *in vivo*, resulted from not only the rapid tumor-specific accumulation but also the combined PTT/PDT/chemotherapy effect. Moreover, minimum systemic toxicity of BPDC NCs ensures their reliable biosafety for clinical applications. Taken together, this proof-of-concept study may enlighten the development of a series of strategies for imaging-guided multimodal tumor therapy by using functional inorganic metal chalcogenides.

Conflict of interest

The authors declare no competing financial interest.

Acknowledgements

P. X. and Y.K. are grateful to the Technology Innovation and Application Demonstration Grant of Chongqing (cstc2018jscx-msybX0078) and National Natural Science Foundation of China (51703186, 31671037).

References

1. Y. Y. Wang, Y. B. Deng, H. H. Luo, A. J. Zhu, H. T. Ke, H. Yang and H. B. Chen, *ACS Nano*, 2017, **11**, 12134-12144.

View Article Online
DOI: 10.1039/C9BM00351G

2. E. Blanco, H. Shen and M. Ferrari, *Nat.Biotechnol*, 2015, **33**, 941-951.

3. W. Gao, B. Xiang, T. T. Meng, F. Liu and X. R. Qi, *Biomaterials*, 2013, **34**, 4137-4149.

4. S. S. Lucky, K. C. Soo and Y. Zhang, *Chem.Rev.*, 2015, **115**, 1990-2042.

5. L. C. Gomes-da-Silva, N. A. Fonseca, V. Moura, M. C. P. de Lima, S. Simoes and J. N. Moreira, *Accounts Chem. Res.*, 2012, **45**, 1163-1171.

6. T. Saleh and S. A. Shojaosadati, *Hum. Vacc Immunother.*, 2016, **12**, 1863-1875.

7. L. Zou, H. Wang, B. He, L. Zeng, T. Tan, H. Cao, X. He, Z. Zhang, S. Guo and Y. Li, *Theranostics*, 2016, **6**, 762-772.

8. N. Nomikou, K. Curtis, C. McEwan, B. M. G. O'Hagan, B. Callan, J. F. Callan and A. P. McHale, *Acta Biomater.*, 2017, **49**, 414-421.

9. N. E. Sounni and A. Noel, *Clin. Chem.*, 2013, **59**, 85-93.

10. D. K. Chatterjee, P. Diagaradjane and S. Krishnan, *Ther. Delivery*, 2011, **2**, 1001-1014.

11. X. N. An, A. J. Zhu, H. H. Luo, H. T. Ke, H. B. Chen and Y. L. Zhao, *ACS Nano*, 2016, **10**, 5947-5958.

12. X. Zhao, C. X. Yang, L. G. Chen and X. P. Yan, *Nat. Commun.*, 2017, **8**.

13. Q. H. Feng, Y. Y. Zhang, W. X. Zhang, X. N. Shan, Y. J. Yuan, H. L. Zhang, L. Hou and Z. Z. Zhang, *Acta Biomater.*, 2016, **38**, 129-142.

14. S. Parvanian, S. M. Mostafavi and M. Aghashiri, *Sens. Biosensing Res*., 2017, **13**, 81-87.

15. S. C. Baetke, T. Lammers and F. Kiessling, *Br. J. Radiol*., 2015, **88**, 20150207.

16. A. S. Thakor and S. S. Gambhir, *CA: Cancer J. Clin*., 2013, **63**, 395-418.

17. C. M. Tempany, J. Jayender, T. Kapur, R. Bueno, A. Golby, N. Agar and F. A. Jolesz, *Cancer*, 2015, **121**, 817-827.

View Article Online
DOI: 10.1039/C9BM00351G

18. K. Kuroda, M. Ye, A. Kimura, S. V. Eremeev, E. E. Krasovskii, E. V. Chulkov, Y. Ueda, K. Miyamoto, T. Okuda, K. Shimada, H. Namatame and M. Taniguchi, *Phys. Rev. Lett.*, 2010, **105**.

19. D. Hsieh, D. Qian, L. Wray, Y. Xia, Y. S. Hor, R. J. Cava and M. Z. Hasan, *Nature*, 2008, **452**, 970-U975.

20. X. D. Zhang, J. Chen, Y. Min, G. B. Park, X. Shen, S. S. Song, Y. M. Sun, H. Wang, W. Long, J. Xie, K. Gao, L. Zhang, S. Fan, F. Fan and U. Jeong, *Adv .Funct Mater.*, 2014, **24**, 1718-1729.

21. Z. L. Li, Y. Hu, K. A. Howard, T. T. Jiang, X. L. Fan, Z. H. Miao, Y. Sun, F. Besenbacher and M. Yu, *ACS Nano*, 2016, **10**, 984-997.

22. Z. H. Song, Y. Z. Chang, H. H. Xie, X. F. Yu, P. K. Chu and T. F. Chen, *NPG Asia Mater.*, 2017, **9**.

23. L. Zhuo, L. Zhenglin, S. Lei, D. Baosheng, W. Yuanlin, Z. Gongyuan, Y. Dengfeng, Y. Sisi, S. Ye and Y. Miao, *Part. Part. Syst .Charact.*, 2018, **35**, 1700337.

24. O. Rabin, J. M. Perez, J. Grimm, G. Wojtkiewicz and R. Weissleder, *Nat. Mater.*, 2006, **5**, 118-122.

25. D. J. Brenner and E. J. Hall, *N.Engl .J .Med.*, 2007, **357**, 2277-2284.

26. P. F. FitzGerald, R. E. Colborn, P. M. Edic, J. W. Lambert, A. S. Torres, P. J. Bonitatibus, Jr. and B. M. Yeh, *Radiology*, 2016, **278**, 723-733.

27. M. S. Kandanapitiye, M. Gao, J. Molter, C. A. Flask and S. P. D. Huang, *Inorg. Chem.*, 2014, **53**, 10189-10194.

28. M. Hernandez-Rivera, I. Kumar, S. Y. Cho, B. Y. Cheong, M. X. Pulikkathara, S. E. Moghaddam, K. H. Whitmire and L. J. Wilson, *ACS Appl. Mater. Interfaces*, 2017, **9**, 5709-5716.

29. S. S. Yang, Z. L. Li, Y. L. Wang, X. L. Fang, Z. H. Miao, Y. Hu, Z. Li, Y. Sun, F. Besenhacher and M. Yu, *ACS applied materials & interfaces*, 2018, **10**, 1605-1615.

View Article Online
DOI: 10.1039/C9BM00351G

30. E. R. Swy, A. S. Schwartz-Duval, D. D. Shuboni, M. T. Latourette, C. L. Mallet, M. Parys, D. P. Cormode and E. M. Shapiro, *Nanoscale*, 2014, **6**, 13104-13112.

31. Z. L. Li, J. Liu, Y. Hu, K. A. Howard, Z. Li, X. L. Fan, M. L. Chang, Y. Sun, H. Besenbacher, C. Y. Chen and M. Yu, *ACS Nano*, 2016, **10**, 9646-9658.

32. E. J. Hong, D. G. Choi and M. S. Shim, *Acta Pharm.Sin. B*, 2016, **6**, 297-307.

33. A. Juarranz, P. Jaen, F. Sanz-Rodriguez, J. Cuevas and S. Gonzalez, *Clin. Transl. Oncol.*, 2008, **10**, 148-154.

34. R. Ideta, F. Tasaka, W. D. Jang, N. Nishiyama, G. D. Zhang, A. Harada, Y. Yanagi, Y. Tamaki, T. Aida and K. Kataoka, *Nano Lett.*, 2005, **5**, 2426-2431.

35. F. Selvestrel, F. Moret, D. Segat, J. H. Woodhams, G. Fracasso, I. M. R. Echevarria, L. Bau, F. Rastrelli, C. Compagnin, E. Reddi, C. Fedeli, E. Papini, R. Tavano, A. Mackenzie, M. Bovis, E. Yaghini, A. J. MacRobert, S. Zanini, A. Boscaini, M. Colombatti and F. Mancin, *Nanoscale*, 2013, **5**, 6106-6116.

36. H. Kato, K. Furukawa, M. Sato, T. Okunaka, Y. Kusunoki, M. Kawahara, M. Fukuoka, T. Miyazawa, T. Yana, K. Matsui, T. Shiraishi and H. Horinouchi, *Lung Cancer*, 2003, **42**, 103-111.

37. T. V. Akhlynina, D. A. Jans, A. A. Rosenkranz, N. V. Statsyuk, I. Y. Balashova, G. Toth, I. Pavo, A. B. Rubin and A. S. Sobolev, *J .Biol. Chem.*, 1997, **272**, 20328-20331.

38. Y. Liu, K. Ma, T. Jiao, R. Xing, G. Shen and X. Yan, *Sci. Rep.*, 2017, **7**, 42978.

39. W. Zhang, J. L. Shen, H. Su, G. Mu, J. H. Sun, C. P. Tan, X. J. Liang, L. N. Ji and Z. W. Mao, *ACS Appl. Mater. Interfaces*, 2016, **8**, 13332-13340.

40. H. Jeong, M. Huh, S. J. Lee, H. Koo, I. C. Kwon, S. Y. Jeong and K. Kim, *Theranostics*, 2011, **1**, 230-239.

41. Z. L. Dong, L. Z. Feng, Y. Hao, M. C. Chen, M. Gao, Y. Chao, H. Zhao, W. W. Zhu, J. J. Liu, C. Liang, Q. Zhang and Z. Liu, *J. Am .Chem .Soc.*, 2018, **140**, 2165-2178.

42. H. Y. Yoon, H. Koo, K. Y. Choi, S. J. Lee, K. Kim, I. C. Kwon, J. F. Leary, K. Park, S. H. Yuk, J. H. Park and K. Choi, *Biomaterials*, 2012, **33**, 3980-3989.

View Article Online
DOI: 10.1039/C9BM00351G

43. S. Kayal and R. V. Ramanujan, *Mater. Sci. Eng., C*, 2010, **30**, 484-490.

44. O. L. Gladkova, M. V. Parkhats, A. N. Gorbachova and S. N. Terekhov, *Spectrochim. Acta, Part A*, 2010, **76**, 388-394.

45. S. Zheng, X. Li, Y. Zhang, Q. Xie, Y. S. Wong, W. Zheng and T. Chen, *Int. J. Nanomed.*, 2012, **7**, 3939-3949.

46. P. Mohan and N. Rapoport, *Mol. Pharmaceutics*, 2010, **7**, 1959-1973.

47. L. Zhao, H. Yang, T. Amano, H. Qin, L. Zheng, A. Takahashi, S. Zhao, I. Tooyama, T. Murakami and N. Komatsu, *J. Mater. Chem. B*, 2016, **4**, 7741-7748.

48. Z. Lin, Y. Liu, X. M. Ma, S. Y. Hu, J. W. Zhang, Q. Wu, W. B. Ye, S. Y. Zhu, D. H. Yang, D. B. Qu and J. M. Jiang, *Sci. Rep.*, 2015, **5**, 11709.

49. H. Xie, Z. Li, Z. Sun, J. Shao, X.-F. Yu, Z. Guo, J. Wang, Q. Xiao, H. Wang, Q.-Q. Wang, H. Zhang and P. K. Chu, *Small*, 2016, **12**, 4136-4145.

50. B. K. Wang, J. H. Wang, Q. Liu, H. Huang, M. Chen, K. Y. Li, C. Z. Li, X. F. Yu and P. K. Chu, *Biomaterials*, 2014, **35**, 1954-1966.

51. Q. W. Tian, F. R. Jiang, R. J. Zou, Q. Liu, Z. G. Chen, M. F. Zhu, S. P. Yang, J. L. Wang, J. H. Wang and J. Q. Hu, *ACS Nano*, 2011, **5**, 9761-9771.

52. W. Y. Yin, L. Yan, J. Yu, G. Tian, L. J. Zhou, X. P. Zheng, X. Zhang, Y. Yong, J. Li, Z. J. Gu and Y. L. Zhao, *ACS Nano*, 2014, **8**, 6922-6933.

53. Y. Wang and Z. Xu, *RSC Adv.*, 2016, **6**, 314-322.

54. F. Yan, W. Duan, Y. Li, H. Wu, Y. Zhou, M. Pan, H. Liu, X. Liu and H. Zheng, *Theranostics*, 2016, **6**, 2337-2351.

55. Y. Ma, X. L. Liang, S. Tong, G. Bao, Q. S. Ren and Z. F. Dai, *Adv .Funct. Mater.*, 2013, **23**, 815-822.

56. G. Kroemer, *Eur. J .Cancer*, 1999, **35**, S307-S307.

57. M. Schieber and N. S. Chandel, *Curr. Biol.*, 2014, **24**, R453-R462.

View Article Online
DOI: 10.1039/C9BM00351G

58. J. Liu, X. P. Zheng, L. Yan, L. J. Zhou, G. Tian, W. Y. Yin, L. M. Wang, Y. Liu, Z. B. Hu, Z. J. Gu, C. Y. Chen and Y. L. Zhao, *ACS Nano*, 2015, **9**, 696-707.

59. H. Lusic and M. W. Grinstaff, *Chem. Rev.*, 2013, **113**, 1641-1666.

View Article Online
DOI: 10.1039/C9BM00351G

Table of contents entry

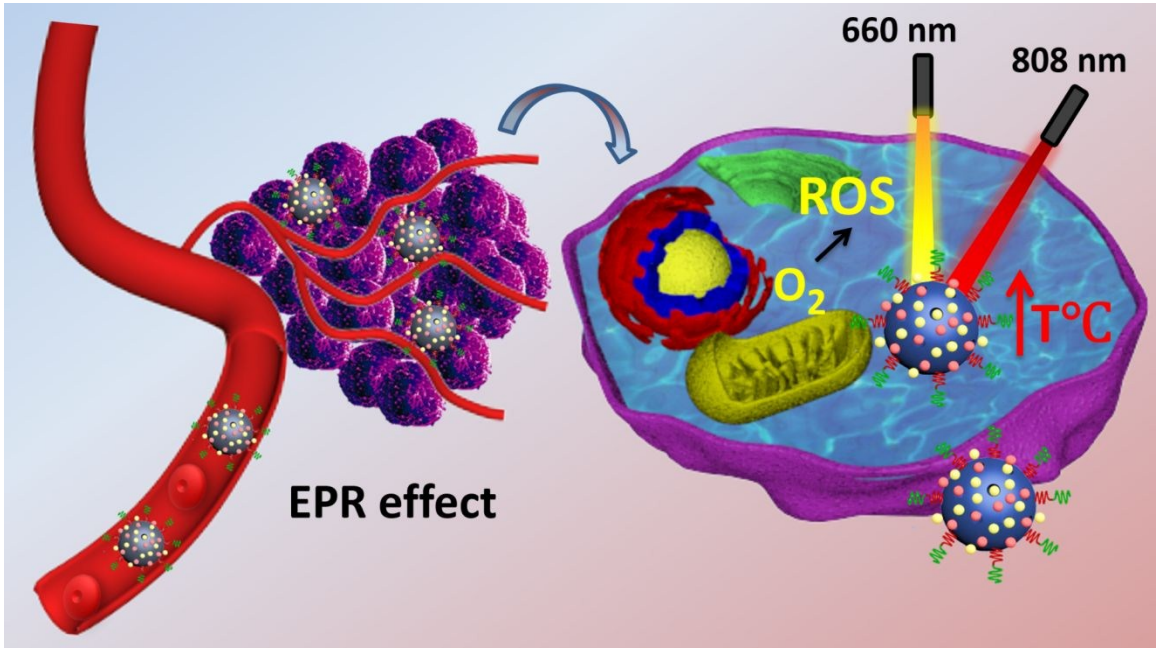

PEGylated bismuth selenide hollow nanocapsules encapsulating doxorubicin and chlorin e6 for fluorescence/CT imaging and light-driven multimodal tumor therapy.